Supporting Information

Amir et al. 10.1073/pnas.1317497111

Microfluidics Setup

The central element of the experimental setup consists of a microfluidic device (the "mother machine"), with dimensions that match well those of the bacteria (width and height of ∼1 μm, matching the bacteria's diameter) (Fig. 1). Details of the fabrication of the devices are described elsewhere (1).

In contrast to the work of ref. 1 where the robustness of the growth was studied and the bacteria were constantly dividing, here we suppress the cell division by regulating proteins involved in the division machinery (SulA for *Escherichia coli* and YlaO for *Bacillus subtilis*), after inserting the cells into the microchannels. Upon filamentation, a single bacterium will fill the 25-μm long channels, and upon further growth, part of the bacterium will be exposed to the flow in the main chamber of the microfluidic device (Fig. 1). In most experiments the flow was of LB broth, which was also used to supply the bacteria with nutrients, but we have also done the experiments using minimal and synthetic rich media (Fig. 5). Next, we will characterize the flow and calculate the resulting forces on the bacteria.

Mapping the Flow Field

Throughout the experiment, the Reynolds number is low enough ($\sim 10^{-2}$) such that the flow is laminar. The bacteria reside very close to the surface, though, where the velocity vanishes, and for this reason it is important to accurately characterize the profile of the flow through the device. In the experimental setup, the pressure on the device is controlled. For a given pressure difference, the flow through the device can be analytically expressed as an infinite series (2). Fig. S1*A* shows the theoretical expectation for the flow through a cross-section of the main channel.

We mapped the flow with spinning-disk confocal microscopy, using fluorescent beads with a diameter of 20 nm and an exposure time of 2 ms. We extracted the velocity profile from the lengths of the tracks left by the beads. A comparison of the measurement and the theoretical expectations, with no fitting parameters, is shown in Fig. S1*B*.

To estimate the drag force on a bacterium (per unit length), we use the exact solution for the viscous drag force (per unit length) on a cylinder residing on a surface (3):

$$f = 4\pi\eta r \frac{\partial v}{\partial z}, \qquad \text{[S1]}$$

where r is the bacterium's radius and $\partial v/\partial z$ is the gradient of the velocity profile close to the surface far away from the cell (where the flow velocity is approximately linear in height above the surface). In our setup, the force is ∼40 pN/μm. In this configuration, the net lift on the cell due the flow can be shown to vanish, but there is a nonvanishing torque per unit length due to the flow (3):

$$\tau_{\text{flow}} = 6\pi\eta r^2 \frac{\partial v}{\partial z}. \qquad \text{[S2]}$$

This torque leads to a nonvanishing σ_{xy} component of the stress tensor. This component, however, is not expected to couple to the cell wall growth and can therefore be neglected. Moreover, the resulting shear stresses obey $\sigma_{xy} 2\pi r^2 = \tau_{\text{flow}}$, and are significantly smaller than the σ_{yy} stress which we shall later calculate. Similarly, σ_{xx} due to the flow is also negligible.

Microscopy and Image Analysis

We used a Nikon TI microscope, with fluorescence light provided by the Lumencore Spectra X arc lamp and a 100× objective. We used the Nikon Perfect Focus system to maintain the cells in focus during each measurement, which typically lasted for 30–60 min for each field of view. Phase contrast images were taken every 1 s, and fluorescent images with a YFP filter were taken every 20 s, to minimize the effects of phototoxicity (in Figs. 2*A* and 3*A* we show that exponential growth with the physiological growth rate is achieved for these conditions: slightly less than 30 min in Fig. 2*A* and approximately 40 min in Fig. 3*A*). For this reason exposure times were chosen as minimal ones that provide good signal-to-noise ratios (SNRs). These were typically 100 ms for the phase contrast images and 20–40 ms for the fluorescent images.

We implemented an image-processing algorithm to track the shape of the cell as a function of time, which was optimized for the purposes of our experiment. The phase contrast images were used to initially find the location of the end of the microchannel (not visible in the fluorescent images), manually. For the image processing, only the fluorescent channel images were used, due to their superior SNR (which was typically between 3 and 5 when comparing the center of the bacterium and the noise level). The algorithm is described in the following.

i) Starting at the end of the microfluidic channel, the position along the cell is followed, where at each running step we keep track of the direction of the local tangent to the cell. Initially, the tangent is pointing in the y direction, as shown in point A in Fig. S2.

ii) At every step of the algorithm, the first approximation to the next tracking point is chosen by taking the current pointer position and advancing it by a small increment (0.067 μm, corresponding to one pixel) in the direction of the current tangent.

iii) The intensity profile is extracted in a line perpendicular to the tangent (see for example the line next to point B in Fig. S2 and Fig. S2, *Inset* showing the corresponding intensity profile). The length of the perpendicular segment is chosen as 1 μm, to match the bacteria's diameter—we shall define it as the "search range." The center of mass of the intensity in the search range is calculated, to minimize the fluctuations, which is chosen as the new pointer position.

iv) The new tangent can now be chosen as the difference between the updated pointer and the pointer from previous runs, where, to avoid large local fluctuations due to noise, we choose to compare two pointers separated by 20 runs (corresponding to ∼1 μm).

v) To find the tip of the bacteria, we define the noise level as the median of the intensity over the entire field of view, and in the previous tracking algorithm we demand that the average intensity over the search range should be greater than a threshold of SNR = 3.

vi) When the signal goes below the threshold, implying we have reached the end of the bacterium, we fit a fourth-order polynomial to the extracted shape, and use the smooth polynomial to calculate the contour length of the bacterium.

Theory of the Elastic Deformations

The Young modulus of peptidoglycan was estimated in refs. 4 and 5 to be of the order of $Y = 3 \times 10^7$ N/m^2. The thickness of the cell wall, h, is of the order of 2 to 4 nm. In a similar fashion to the usual derivation of the deformation of an elastic rod, we can calculate the elastic deformation of a hollow rod of thickness

$h \ll r$, subject to a constant force per unit length perpendicular to its axis of symmetry. This is equivalent to the problem of a rod being deformed under its own weight, with one fixed end and one free end (ref. 6, p. 81). We outline the details of the calculation, because part of the reasoning will also be relevant to the discussion of the irreversible deformations in *Theory of Plastic Deformations*. A key ingredient is the (geometric) connection between the local radius of curvature and the local strains. As illustrated in Fig. S3, for a given radius of curvature $R(y)$ at a given point y along the cell, the strain on a smaller region of the outer part of the cell wall will be given by

$$\frac{\delta l}{dl} = \frac{dl_2 - dl_1}{Rd\varphi} \approx 2r/R, \qquad \textbf{[S3]}$$

where $dl = Rd\varphi$ is the arc traversed by the centerline.

Here, we assume that the strains vanish for a straight cell, an assumption that will not hold when we will consider asymmetric insertions in *Theory of the Plastic Deformations*. We also assumed that the strains are small, which does not imply that the deflections are small—for a cell with a large aspect ratio, one can have small strains throughout the cell leading to an overall large angular deflection. The typical deflections $\delta(y)$ calculated below are in the range $r \ll \delta(y) \ll l$, where l is the protruding length of the bacterium. In the regime of linear elasticity, the strains are proportional to the stresses. The surrounding viscous flow creates primarily a σ_{yy} component of the stress tensor within the cell wall (see Fig. 1 for the definition of the coordinate system), which can be found from the condition that the torques created by them must compensate for the torque created by the external forces. We proceed to express the extra stress at a point with coordinate y along the centerline of the cell's long axis and azimuthal angle θ, in terms of the flow parameters (see Fig. S8 for the definition of θ). Using the linear relation of stress and strain in a hollow rod (6), we expect that for small deformations

$$\sigma_{yy}(\theta, y) \approx Yr \sin(\theta)/R(y), \qquad \textbf{[S4]}$$

where $R(y)$ is the local radius of curvature (not to be confused with the radius of the bacteria, r), and Y is the Young modulus of the cell wall. Upon balancing the torque induced by this stress with the external torque at position y, $\tau(y)$, we find that

$$\tau(y) = \frac{Y\,I}{R(y)}, \qquad \textbf{[S5]}$$

where I is the moment of inertia of a cross-section, which for our case is found to be $I = \pi r^3 h$ [this result can also be obtained by differentiating the formula for a solid cylinder, $I_s = (\pi/4)r^4$]. Note that the moment of inertia is a mathematical analogy with the theory of rigid bodies, a notation commonly used in the theory of rod elasticity. $Y\,I$ is known as the flexural rigidity. For a constant force per unit length f we find that the stresses within the cell wall are

$$\sigma_{yy}(\theta, y) = \frac{f \sin(\theta)(y-l)^2}{2\pi r^2 h}. \qquad \textbf{[S6]}$$

This result should be multiplied by the thickness h if one is interested in the 2D stress. Indeed, one can check directly that the torques arising from these stresses at a cross-section at point y are equal to the total torque due to the force f integrated along the segment $[y, l]$. Upon combining Eqs. **S6** and **S4**, the resulting curvature is given by

$$1/R(y) \approx \frac{f(y-l)^2}{2Y\,I}. \qquad \textbf{[S7]}$$

We note from differential geometry that the radius of curvature can be expressed in terms of the horizontal deflection of the bacterium $\delta(y)$, as

$$\frac{1}{R} = \frac{\delta''}{\left(1+\delta'^2\right)^{3/2}}. \qquad \textbf{[S8]}$$

Upon neglecting the δ' term in the denominator, valid for weak deflections, and focusing on the case of a constant force along the cell, we obtain a linear equation that can be readily integrated to give the resulting deflection of a point y along the cylinder. Under the assumption of a vanishing derivative at the end of the microchannel, we find that

$$\delta(y) = \frac{fy^2\left(y^2 - 4ly + 6l^2\right)}{24Y\,I}. \qquad \textbf{[S9]}$$

Thus, the maximal deflection $\delta_{\max} = \delta(y = l)$ is given by

$$\frac{\delta_{\max}}{l} = \frac{fl^3}{8Y\,I}. \qquad \textbf{[S10]}$$

We conclude that the horizontal deformation of the tip $\delta(l)$ is approximately proportional to l^4, where l is the length of the cell exposed to the force. Based on the data in Fig. 2*B*, we were able to calculate the stiffness of the *E. coli* cells, and extract a flexural rigidity of 4×10^{-20} to 6×10^{-20} N·m^2. This result is similar to that obtained by very different methods, such as atomic force microscopy (4) and recent work in which the cells were transiently deformed by optical traps (7). It should be pointed out that even though the perpendicular deflections are significant, the local strains and stresses are in fact small. Thus, it is justified to assume that we are in the regime of linear elasticity. Due to the large aspect ratio of the filamentous bacteria, whose length l is much larger than their radius r, the deflections are enhanced by a factor of l/r.

Recently, bending of elastic fibers in a flow was studied, experimentally and theoretically, albeit in a different regime of parameters where the flow is highly confined and the fiber blocks most of it (8).

The Effect of the Bacterium/Microchannel Mismatch on Elastic Measurements

The previous analysis of the elastic deformations assumed a boundary condition with the cell fixed at the end of the microchannel, i.e., that the tangent to the cell centerline would be parallel to the microchannel there. However, looking at a typical cell (for example, Fig. S4) shows that there can be a finite derivative $\delta'(y=0) = a$ there, due to the small mismatch between the cell diameter and the channel diameter at the end of the microchannel, which we denote by Δ.

We will find a by analyzing the forces and torques, show that the assumption of a cell fixed at the microchannel end is an excellent one for the longer cells, and account for the deviations for the shorter cells.

The torque balance for the part of the cell outside the microchannel implies that y'' is still given by Eq. **S7**, and thus the shape of the cell is given by

$$\delta(y) = \frac{fy^2\left(y^2 - 4ly + 6l^2\right)}{24Y\,I} + ay, \qquad \textbf{[S11]}$$

where a is yet to be determined. For the part of the cell inside the microchannel, external forces F_1 and F_2 are only applied at two points (shown in Fig. S4). The derivative at the point where F_2 is applied vanishes (because the cell is tangent to the microchannel there), so the position of the centerline of the cell is given by the usual solution of a beam bent by an external force (6, 7):

$$\delta(y)=\frac{F_2}{Y\,I}\left(\frac{y_0(y_0+y)^2}{2}-\frac{(y_0+y)^3}{6}\right),\quad -y_0\le y\le 0 \qquad \textbf{[S12]}$$

where $y=0$ corresponds to the end of the microchannel. We therefore have

$$\Delta=\frac{F_2}{3Y\,I}y_0^3. \qquad \textbf{[S13]}$$

However, both F_2 and y_0 are unknown. We fix these quantities by considering the torques around the end of the microchannel:

$$F_2y_0=\tau=\int_0^l fl'dl'=fl^2/2. \qquad \textbf{[S14]}$$

Upon eliminating F_2 from Eqs. **S13** and **S14**, we find that

$$\frac{1}{3Y\,I}y_0^2=\frac{\Delta}{\tau}. \qquad \textbf{[S15]}$$

Hence

$$y_0=\sqrt{\frac{3Y\,I\Delta}{\tau}},\quad F_2=y_0/\tau=\frac{2y_0}{fl^2}. \qquad \textbf{[S16]}$$

Because the derivative at the end of the microchannel is continuous, we have

$$a=\sqrt{\frac{3\Delta\tau}{4Y\,I}}=\sqrt{\frac{3\Delta fl^2}{8Y\,I}}. \qquad \textbf{[S17]}$$

For the case of a perfect match between the bacterium and the microchannel diameter ($\Delta=0$), the maximal deflection was given by

$$\delta_{\max}=\frac{fl^4}{8Y\,I}. \qquad \textbf{[S18]}$$

The corrected maximal deflection will now be

$$\delta_{\max}=\frac{fl^4}{8Y\,I}+l^2\sqrt{\frac{3f\Delta}{8Y\,I}}. \qquad \textbf{[S19]}$$

The correction is negligible for long enough cells, $l\ge(24Y\cdot I/f)^{1/4}$, but becomes significant for short cells. It is also possible to take into account a nonuniform force per unit length outside the channel: In this case, the force per unit length f and torque τ must be recalculated as a function of position on the cell. The deflection can then be calculated by numerical integration. Fig. 2*B* uses this more general procedure when modeling the elastic deformations:

i) We use the full solution for the flow profile to calculate the force per unit length at every point along the cell, and the resulting torques at every point.

ii) We solve the elastica problem for this torque distribution, and find the resulting deflection by integrating the equations numerically, including the nonlinear terms due to the denominator of Eq. **S8.**

For stiff, long cells using Eq. **S19** with a constant force per unit length $f\approx 40$ pN/μm would be an excellent approximation because the flow would be approximately constant and the deformations of stiff cells would be still small such that the nonlinear contributions are insignificant. This is the case for the data shown in Fig. S6.

Simple and Noninvasive Measurements of Young's Modulus

Transient bending by pulse-like forces provide simple, noninvasive means to directly measure the elastic properties of living bacterial cells. Fig. S6 shows the maximum deflection $\delta_{\max}$ vs. the length (l) of the cells exposed to the force. The solid red line is the fit using a full theoretical flow profile in Fig. S1, and we obtained the flexural rigidity $Y\,I\approx 2.4\times10^5$ pN·μm^2. This implies $Y\approx 20.4$ MPa for a cell radius $r=0.5$ μm and a cell wall thickness $h=30$ nm, in good agreement with past measurements which found Y = 10–50 MPa (9–11).

We also used Eq. **S19** to fit both the average force per unit length, f, and the flexural rigidity (Δ can be measured directly from Fig. S4). We obtain a fit that is virtually identical to the full flow result (Fig. S6). For $\Delta=0.5$ μm, we find $f\approx 41.2$ pN/μm and $Y\,I\approx 2.1\times10^{-19}$ N·m^2. With the same assumptions from above we find $Y\approx 19.9$ MPa, consistent with the results using the full flow profile. This suggests that our flow-based scheme of imparting force may provide a simple and robust measurement of the Young's modulus of various bacteria.

The Lack of Torque Due to Turgor Pressure

Turgor pressure creates no torque on the cell, and for this reason need not be taken into account throughput the analysis. To show this, consider an integral over the closed red cross-sectional contour surface sketched in Fig. S5. The force and torque due to these forces must vanish because the material inside is in mechanical equilibrium. In the analysis of cell wall deformations, one has to find the torque exerted on the cell wall by external forces. The contribution to this torque by the turgor pressure around point A in Fig. S5, for example, is exactly that associated with the above contour, except for the missing additional torque associated with the flat surface inside the cell (denoted by the dashed line in the figure). The forces there, however, give rise to a negligible torque because they have no lever arm. We conclude that the torque due to turgor pressure around any point along the cell would vanish. The only effect of the pressure is thus to create large stresses σ_{xx} and σ_{yy} in the cell wall.

Theory of the Plastic Deformations

We will now estimate the rate of bending due to the asymmetric synthesis of cell wall as a response to an external stress (due to the viscous flow). This asymmetry gives rise to an additional bending mechanism, which is irreversible because it involves the remodeling of the peptidoglycan mesh. We will assume that we are still in a regime where the bending is relatively small, so we can use the previous results for the flow around a straight cylinder, and for the forces on a slightly deformed rod. For simplicity of the analysis, let us start by assuming that the Young modulus is large enough such that elastic bending is negligible; we shall see that even for $Y\to\infty$ the plastic bending is finite. In *Shape of a Plastically Deformed Cell* we will explain how the calculation can be extended to take both elastic and irreversible plastic deformations into account.

Consider a cross-section of the bacterium, at a distance y away from the end of the microchannel, as illustrated in Fig. S8. The 2D stress due to the turgor pressure p is independent of θ, and given by $\sigma_{yy}^0=pr/2$. Eq. **S6** shows that the additional stress σ_{yy} due to the viscous drag is positive for $0<\theta<\pi$,

corresponding to the stretched part of the rod, and negative otherwise. The maximal relative change in the stress occurs at the points $\theta = \pm\pi/2$ and $y = 0$ (corresponding to the end of the microchannel) and equals

$$\Delta\sigma/\sigma_{\text{turgor}} = \pm\frac{fl^2}{\pi pr^3}. \quad \textbf{[S20]}$$

Upon inserting the numbers for a relatively long filamentous bacterium of length 10 μm, we find a ratio of order unity. Thus, the flow can induce significant changes in the stress, for long cells.

We shall now invoke the formalism of the dislocation-mediated growth developed in ref. 12, which hinges on the fact that new material is inserted circumferentially via the rotating strand-extension centers. The σ_{yy} stress induces a Peach–Koehler force on an edge dislocation with a Burgers vector in the y direction, acting in a tangential direction (in the xz plane), $F = b\sigma_{yy}$, as discussed in *Theoretical Framework for Coupling Mechanical Stresses to Cell Wall Growth* in the main text. This force acts in addition to the always-positive stress σ^0_{yy} due to turgor pressure. Tensile stresses enhance growth whereas compressive stresses inhibit it. Under the assumption that the additional stresses are small compared with that due to turgor pressure, we can Taylor expand the dependence of local growth rate on stress, and find

$$\Delta g/g = f\left[\sigma_{yy}\Big/\sigma^0_{yy}\right] \approx \alpha\frac{\sigma_{yy}}{pR/2}, \quad \textbf{[S21]}$$

where the coefficient α multiplying the excess stress σ_{yy} due to bending is expected to be of order unity. Upon inserting the additional stress when a force f per unit length is exerted on the cell, we find that

$$\Delta g/g \approx \alpha\frac{fl^2}{2\pi pr^3}, \quad \textbf{[S22]}$$

(where we take $y = l/2$).

This differential growth, accumulated over time, will turn out to give a nonnegligible plastic deflection even when $\Delta g/g \ll 1$, due to the large aspect ratio of the filamentous bacterium. The bending of the cell will be such that the additional strains corresponding to the bending will compensate those due to the differential growth: Locally, the ratio of arcs dl_2/dl_1 in Fig. S3 should correspond to the relative amount of material incorporated into the cell wall. Let us denote the integrated differential growth arising Eq. **S22** by Δl. The radius of curvature R resulting from the differential growth (Fig. S3) obeys

$$\Delta l/dl \approx (dl_2 - dl_1)/dl_1 = 2r/R, \quad \textbf{[S23]}$$

leading to a curvature $\kappa \equiv 1/R = \frac{1}{2r}\Delta l/dl$. The angle $d\varphi$ resulting from this differential growth obeys $Rd\varphi = dl$, hence

$$d\varphi = \frac{dl}{2r}\Delta l/dl. \quad \textbf{[S24]}$$

Indeed, we find that the relative growth asymmetry of $\Delta l/dl$ is enhanced by the geometrical factor of $dl/2r$. For a long cell with a constant differential growth, this factor would correspond to half the aspect ratio. Note, however, that this argument gives the local curvature due to differential growth, which in our experiments is nonconstant along the length of the cell. These results can be also obtained via differential geometry, by considering the Gaussian curvature associated with the nonuniform metric due to differential growth.

We thus expect that as the bacterium grows to length l, the angle associated with the plastic bending (as long as it is small) should scale as

$$\phi \propto \frac{\Delta l}{l}\frac{l}{2r} \sim \frac{fl^3}{pr^4}. \quad \textbf{[S25]}$$

Upon comparing this angle to that of the elastic deformations (Eq. **S10**), we find that both elastic and plastic effects have the same scaling with l, allowing for a quantification of their relative importance in terms of a single dimensionless parameter:

$$\chi \equiv \frac{pr}{Yh}. \quad \textbf{[S26]}$$

For large enough Y, the plastic effect dominates over the elastic one. With estimated values for *E. coli*, we find that χ is of order unity, implying that elastic and plastic effects are of the same order of magnitude. Thus, one has to solve the coupled problem, without separating the discussion into an elastic and plastic part, as we have so far. For bacteria with stiffer cell walls, we expect the plastic effect to dominate over the elastic one.

Finally, we note that when going from Eq. **S22**, giving the instantaneous relative growth, to the integrated asymmetry Δl, one should also take into account the effect of a finite processivity, which in the absence of differential growth would lead to an exponential decay of the curvature (13). The accumulated relative differential growth $\rho \equiv \Delta l/dl$ obeys

$$\frac{d\rho}{dt} = -\lambda\rho + \alpha\frac{\sigma_{yy}}{pR}\lambda, \quad \textbf{[S27]}$$

where λ is the growth rate [i.e., the doubling time equals $t_d = \log(2)/\lambda$], the first term corresponds to the dilution effect due to the finite procreativity (taken as infinite in the above equation, for simplicity), and the second term corresponds to Eq. **S21**.

Straightening After Snap-Back

The straightening described in the main text (Fig. 3 and Movie S2) is in sharp contrast to the results of ref. 14, where curved, arc-shaped cells taken out of microfluidic channels do not seem to straighten as they grow, but rather, maintain a self-similar shape with a slowly decreasing radius of curvature as they become larger. In fact, the latter is precisely what is expected from circumferential insertions with long processivity (15, 16): Circumferential insertions would dilute the asymmetry due to differential growth and thus lower the curvature, yet because the cell grows longer, the shape can be shown to be self-similar. Taking into account a finite processivity of insertions would make the decay of the curvature slower (13). Therefore, if processive insertions alone are responsible for straightening, during continued growth the tip should move toward the bending direction (→). In contrast, the cells after the partial snap-back, however, actually move toward (←) the channel the bent cell is embedded in (Fig. 3*B*).

Note that due to the turgor pressure, the stress on the cell wall during the straightening process is nonuniform, and one should also take the coupling of the stress distribution to the growth. However, when a cell is deformed, the stress component along the bacterium's long axis (σ_{yy}) remains approximately constant, whereas it is the circumferential component of the stress tensor that is modified, in a manner proportional to the curvature of the bent cell (13, 17). There are no indications that this stress component is coupled to the growth process. We therefore conclude from our experiments that another mechanism is at play, which makes the cell straightening significantly faster in the absence of mechanical forces. One possibility is a curvature-sensing mechanism that has been discussed in the context of protein localization in bacteria (18). A second mechanism is the appearance of residual stresses due to the differential growth in the first stage of the experiment: The combination of turgor pressure and the differential growth can lead to residual stresses in the cell wall, which remain even after the flow is turned off, and are in general nonuniform.

Plastic Deformation Relies on Cell Growth

In the main text we demonstrate that plastic deformation of growing cells results from the application of flow-generated hydrodynamic force over extended periods of time. We further demonstrate that, in the time after the flow is stopped, the cells straighten as they grow. We attribute this behavior to a dislocation-mediated growth mechanism in which anisotropic stresses give rise to varying cell wall synthesis rates which leads to plastic deformation.

A remaining possibility, however, is that this plastic deformation is disconnected from growth and the cell wall passively reorganizes (deforms) in response to the anisotropic stresses. To eliminate this mechanism we ran two separate controls. First, we show that nongrowing cells do not plastically deform after extended application of flow (Fig. S7*A*).

Second, we demonstrate that cells grown in (and plastically deformed by) flow do not straighten over time (Fig. S7*B*). Taken together and in contrast to Fig. 3, these experiments indicate that the plastic deformation quantified in this paper is connected to growth of the cell, consistent with a dislocation-mediated growth mechanism.

Shape of a Plastically Deformed Cell

We have shown above that filamentous bacteria will have significant elastic as well as irreversible bending at a length 10–20 μm. In this section we explain how both of the effects can be quantitatively combined to calculate the shape of the cell at a given point.

For the elastic effect, the radius of curvature at a given point is proportional to the strain at that point. For the irreversible effect, it is proportional to the nonuniformity in insertion rates on the two sides of the bacterium (relative to the flow direction). Because both effects turn out to be of the same order of magnitude for the experimentally relevant case, we have to consider both contributions simultaneously. Upon repeating the previous arguments, we find that

$$\frac{1}{R(y)}=\frac{1}{R_e(y)}+\frac{1}{R_i(y)}, \qquad \textbf{[S28]}$$

i.e., the curvature is the sum of the elastic (reversible) and growth-induced (irreversible) contributions. The elastic contribution is given by Eq. **S5**:

$$\frac{1}{R_e(y)}=\frac{\tau(y)}{Y\,I}, \qquad \textbf{[S29]}$$

where $\tau(y)$ is the torque due to the flow, whereas the growth-related contribution is given by Eq. **S23**:

$$\frac{1}{R_i(y)}=\frac{1}{2r}\frac{\Delta l(y)}{dl}. \qquad \textbf{[S30]}$$

We can now quantitatively analyze the experimental scenario: At every point in time we calculate the resulting torque τ due to the flow. This torque gives rise to an elastic curvature (as quantified in Eq. **S29**), which is an instantaneous effect. It will also give rise to a nonuniform insertion rate, which, integrated over time (Eq. **S27**), will give rise to the irreversible component of the curvature (as quantified in Eq. **S30**). Note that a given point on the cell elongates exponentially in time, and that when calculating the accumulated asymmetry $\Delta l/dl$ at a given point we have to follow the path of the point over time, and integrate the contribution of the stresses at different points in space and time, associated with the "history" of that part of the cell wall. For example, the part of the bacterium which is close to the end of the side channels had no stress on it while it was in the channel, and for this reason accumulated no asymmetry: It will have no radius of curvature associated with the irreversible effect. It will have, however, the maximal radius of curvature associated with the elastic contribution because the torque at that point is maximal. Fig. S9 shows the relative contributions of both effects, for realistic experimental parameters.

1. Wang P, et al. (2010) Robust growth of Escherichia coli. *Curr Biol* 20(12): 1099–1103.
2. Hashmi SM, Loewenberg M, Dufresne ER (2007) Spatially extended FCS for visualizing and quantifying high-speed multiphase flows in microchannels. *Opt Express* 15(10): 6528–6533.
3. Schubert G (1967) Viscous flow near a cusped corner. *J Fluid Mech* 27(4):647–656.
4. Yao X, Jericho M, Pink D, Beveridge T (1999) Thickness and elasticity of gram-negative murein sacculi measured by atomic force microscopy. *J Bacteriol* 181(22):6865–6875.
5. Deng Y, Sun M, Shaevitz JW (2011) Direct measurement of cell wall stress stiffening and turgor pressure in live bacterial cells. *Phys Rev Lett* 107(15):158101.
6. Landau LD, Lifshitz EM (1986) *Theory of Elasticity* (Pergamon, New York).
7. Wang S, Arellano-Santoyo H, Combs PA, Shaevitz JW (2010) Actin-like cytoskeleton filaments contribute to cell mechanics in bacteria. *Proc Natl Acad Sci USA* 107(20): 9182–9185.
8. Wexler JS, et al. (2013) Bending of elastic fibres in viscous flows: The influence of confinement. *J Fluid Mech* 720:517–544.
9. Thwaites JJ, Mendelson NH (1989) Mechanical properties of peptidoglycan as determined from bacterial thread. *Int J Biol Macromol* 11(4):201–206.
10. Thwaites JJ, Surana UC (1991) Mechanical properties of Bacillus subtilis cell walls: Effects of removing residual culture medium. *J Bacteriol* 173(1):197–203.
11. Mendelson NH, Sarlls JE, Wolgemuth CW, Goldstein RE (2000) Chiral self-propulsion of growing bacterial macrofibers on a solid surface. *Phys Rev Lett* 84(7):1627–1630.
12. Amir A, Nelson DR (2012) Dislocation-mediated growth of bacterial cell walls. *Proc Natl Acad Sci USA* 109(25):9833–9838.
13. Sliusarenko O, Cabeen MT, Wolgemuth CW, Jacobs-Wagner C, Emonet T (2010) Processivity of peptidoglycan synthesis provides a built-in mechanism for the robustness of straight-rod cell morphology. *Proc Natl Acad Sci USA* 107(22):10086–10091.
14. Takeuchi S, DiLuzio WR, Weibel DB, Whitesides GM (2005) Controlling the shape of filamentous cells of Escherichia coli. *Nano Lett* 5(9):1819–1823.
15. Mukhopadhyay R, Wingreen NS (2009) Curvature and shape determination of growing bacteria. *Phys Rev E Stat Nonlin Soft Matter Phys* 80(6 Pt 1):062901.
16. Jiang H, Sun SX (2012) Growth of curved and helical bacterial cells. *Soft Matter* 8(28):7446–7451.
17. Fluegge S (1973) *Stresses in Shells* (Springer, Berlin).
18. Ramamurthi KS, Lecuyer S, Stone HA, Losick R (2009) Geometric cue for protein localization in a bacterium. *Science* 323(5919):1354–1357.

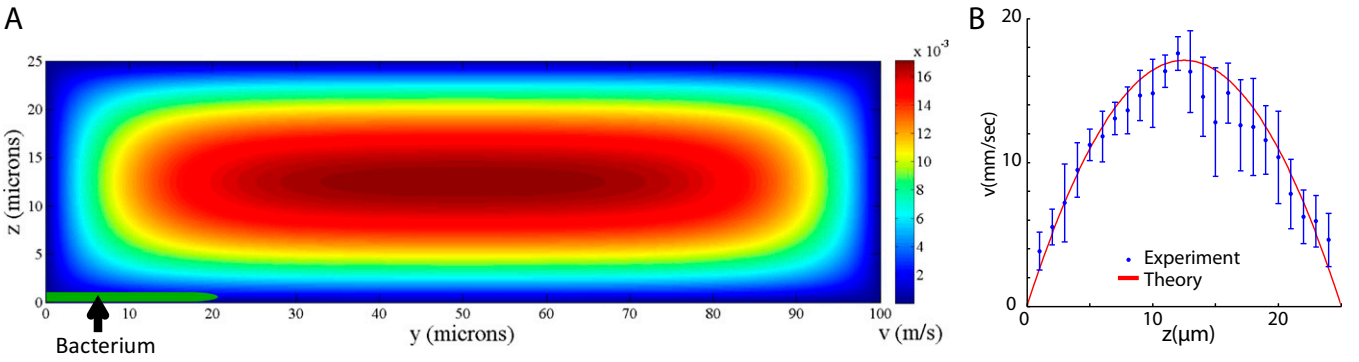

Fig. S1. (*A*) The results of the analytical solution for the flow through the device. A green bacterial cell protruding approximately 20 μm into the chamber is superimposed on the flow field at the lower left. (*B*) Comparison of the measured flow profile, averaged over the width of the device (along the *y* axis), vs. the theoretical expectation for a pressure difference of 3 kPa. The error magnitude was determined according to the uncertainty in determining the position of the beads used to map the flow.

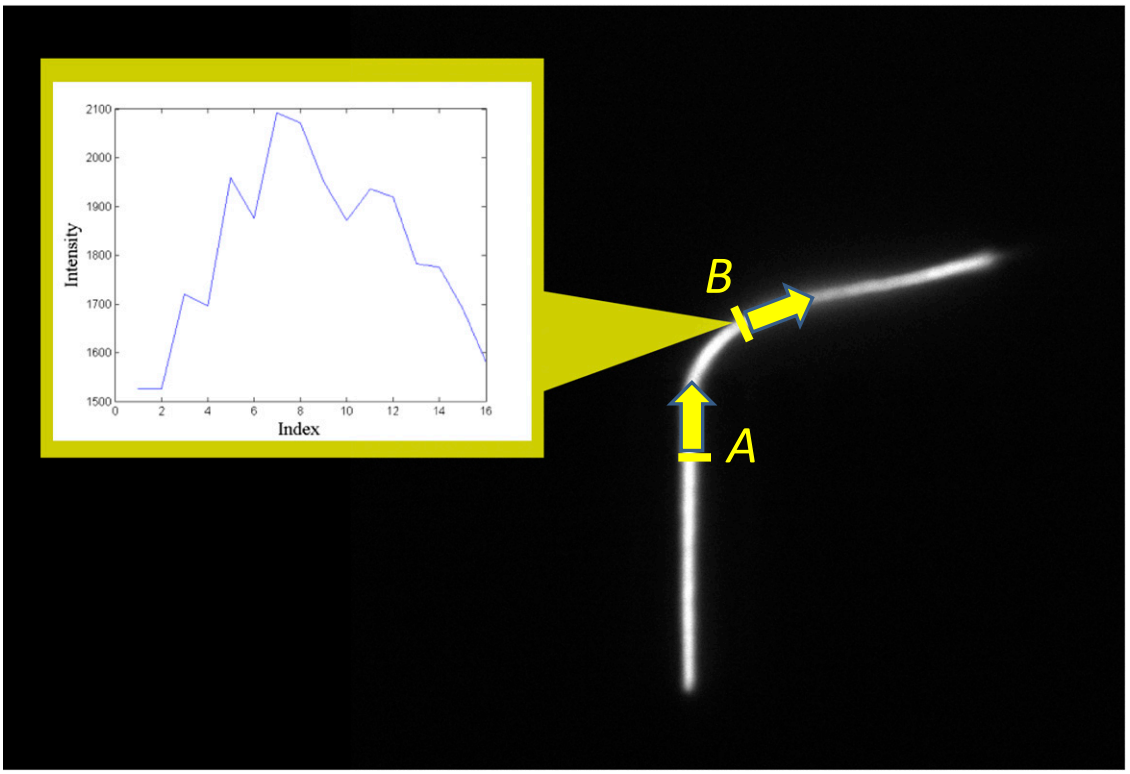

Fig. S2. Schematic illustration of the image processing algorithm used for the analysis. Shown is a raw fluorescent image, adjusted in Adobe Photoshop using autolevels for clarity. Starting at point A (the end of the microchannel), at each point the direction of the local tangent is kept [initially in the direction of the microchannel (yellow arrow)]. The intensity profile in a narrow strip perpendicular to the tangent is calculated (*Inset* showing the profile associated with point B, reached by the algorithm in a later step), and its center of mass is used to update the next point as well as the tangent vector.

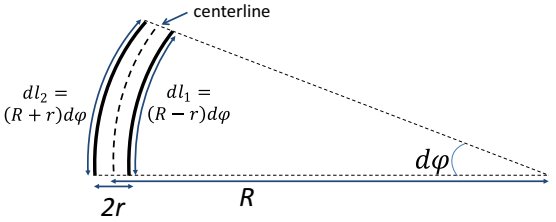

Fig. S3. A small section of a bent cell.

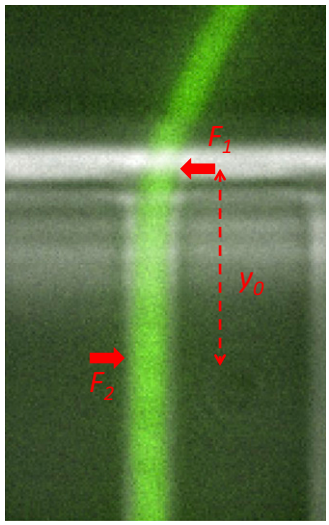

Fig. S4. Forces on a bacterium confined in a channel.

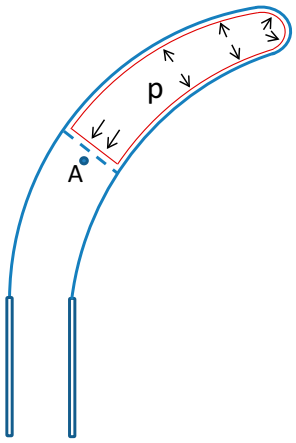

Fig. S5. Turgor pressure exerting forces on a closed contour just inside the cell wall of a protruding bacterium. Cross-section of a growing bacterium; *p* denotes the turgor pressure acting on the cell wall. In the text, the torque around point A due to the turgor pressure is calculated, and is shown to vanish. (The dotted line is an aid to the argument used in the proof.)

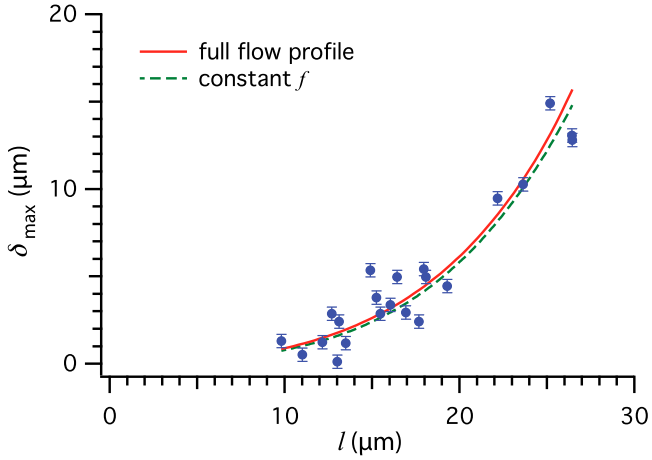

Fig. S6. Elastic measurements of *B. subtilis*. Cells were filamented in the absence of flow and perturbed with brief ~15-s pulses of media flow. The resulting maximum displacements δ_{max} are plotted as a function of the exposed cell length l for the elastic deformations. The red line shows the elastic theory results using the full nonlinear flow profile (in analogy to Fig. 2 for *E. coli*), yielding $Y\,I \approx 2.4 \times 10^{-19}$ N·m^2. The green dashed line is a fit to Eq. **S19**; holding $\Delta = 0.5$ μm, we find $f \approx 41.2$ pN/μm and $Y\,I \approx 2.1 \times 10^{-19}$ N·m^2. Error bars are propagated from the uncertainty in calculating cell tip and channel end positions during image analysis.

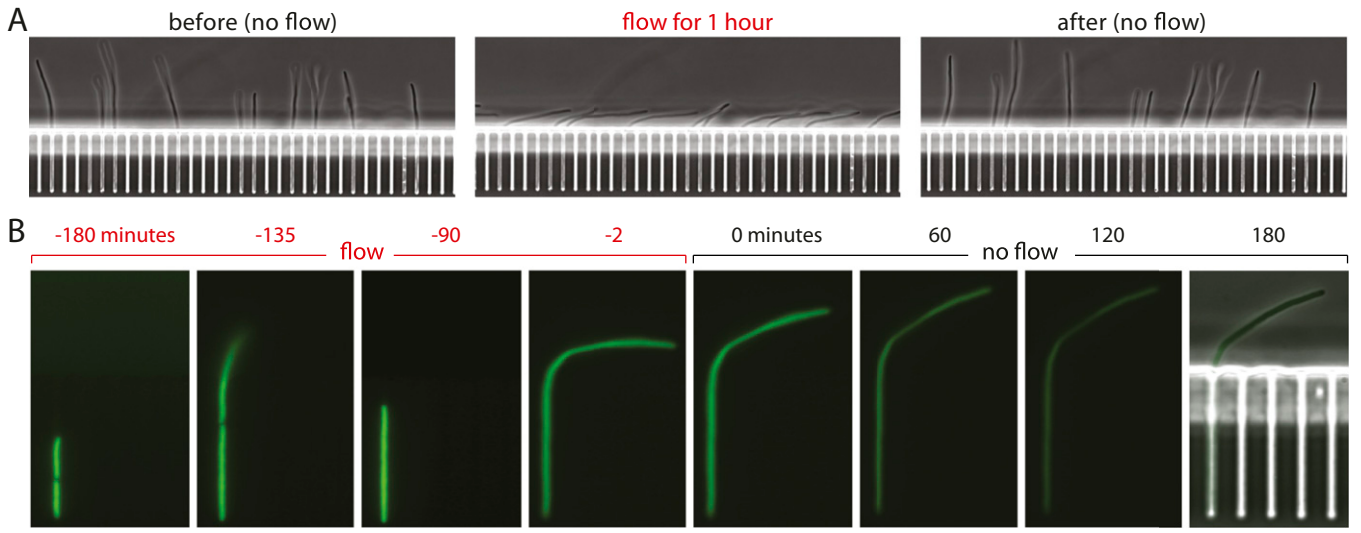

Fig. S7. Controls: Nongrowing cells do not plastically deform. (*A*) Montage showing that nongrowing cells do not deform plastically under flow. *E. coli* cells are filamented in the absence of flow until they protrude from the channels by ~25 μm. At that point, we begin excessive fluorescent illumination and the cells stop growing within 20 min. We then initiate flow, bending the cells, and maintain constant flow for 1 h. After this period we stop the flow and the cells snap-back and fully recover their shape. Thus, nongrowing cells do not deform plastically and the Stokes force during our experiments does not mechanically damage the cells. (*B*) Montage showing that nongrowing cells do not straighten. Filamentation is induced in an *E. coli* cell and it grows in the presence of flow until $t = 0$. Beginning at $t = -24$ min, the cell is exposed to excessive fluorescent illumination which continues for the remainder of the experiment, inhibiting growth. At $t = 0$, snap-back was performed by arresting the flow. From $t = 60$–180 min, the cell shows no appreciable growth, intracellular GFP is photo-bleaching, and the cell does not straighten. In the final frame, a phase-contrast image is overlaid, showing the channels and the cell outline.

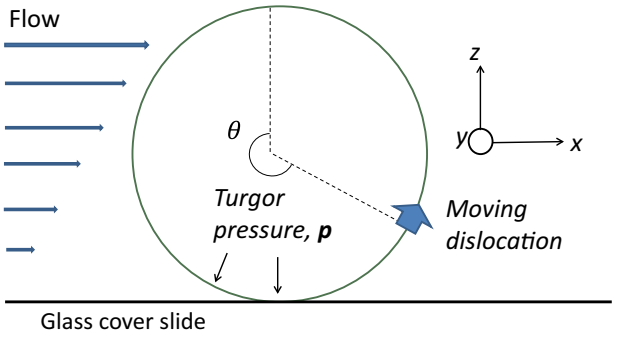

Fig. S8. Cross-section of a growing bacterium.

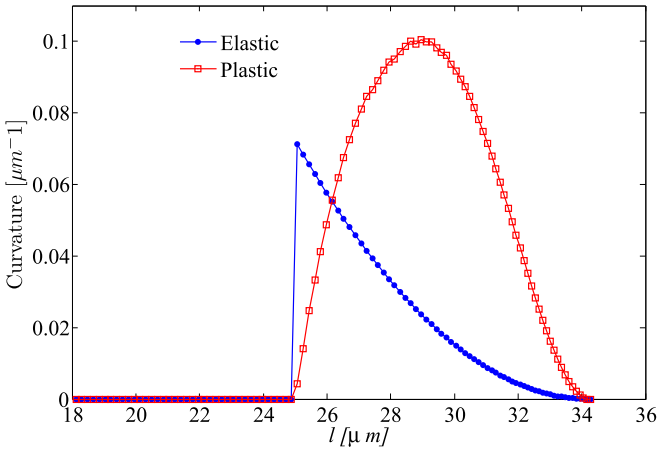

Fig. S9. Contribution of the elastic (reversible) and plastic (irreversible) effects to the cell curvature, as found by numerically solving the coupled equations for differential growth and for the elastic response, with $\alpha = 2.5$ in Eq. **S21**. The elastic effect is maximal just outside the microfluidic channel, where the stresses are maximal, and vanishes at the stress-free tip of the bacterium. The plastic effect, on the other hand, relies on the accumulation of differential growth over time, and therefore vanishes both at the stress-free tip and at the end of the microfluidic channel, which contains a "fresh" cell wall with no asymmetry, having just come out of the microfluidic channel.

Table S1. Summary of parameters for calculating χ for *E. coli* and *B. subtilis*

Parameter	*E. coli*	Source	*B. subtilis*	Source
p	0.3 and 2–3 atm	Refs. 1 and 2	20 atm	Ref. 3
r	0.3–0.5 μm	Ref. 4	0.4 μm	Ref. 5
Y	30 MPa	Refs. 1 and 6 and the present work	10–30, 50, and 20 MPa	Refs. 7 and 8, ref. 9, and the present work
h	1.5–6.5 nm	Ref. 10	30 nm	Ref. 11

1. Deng Y, Sun M, Shaevitz JW (2011) Direct measurement of cell wall stress stiffening and turgor pressure in live bacterial cells. *Phys Rev Lett* 107(15):158101.
2. Koch AL (1990) The surface stress theory for the case of Escherichia coli: The paradoxes of gram-negative growth. *Res Microbiol* 141(1):119–130.
3. Whatmore AM, Reed RH (1990) Determination of turgor pressure in Bacillus subtilis: A possible role for K+ in turgor regulation. *J Gen Microbiol* 136(12):2521–2526.
4. Zaritsky A, Woldringh CL (1978) Chromosome replication rate and cell shape in Escherichia coli: Lack of coupling. *J Bacteriol* 135(2):581–587.
5. Maass S, et al. (2011) Efficient, global-scale quantification of absolute protein amounts by integration of targeted mass spectrometry and two-dimensional gel-based proteomics. *Anal Chem* 83(7):2677–2684.
6. Yao X, Jericho M, Pink D, Beveridge T (1999) Thickness and elasticity of gram-negative murein sacculi measured by atomic force microscopy. *J Bacteriol* 181(22):6865–6875.
7. Thwaites JJ, Mendelson NH (1989) Mechanical properties of peptidoglycan as determined from bacterial thread. *Int J Biol Macromol* 11(4):201–206.
8. Thwaites JJ, Surana UC (1991) Mechanical properties of Bacillus subtilis cell walls: Effects of removing residual culture medium. *J Bacteriol* 173(1):197–203.
9. Mendelson NH, Sarlls JE, Wolgemuth CW, Goldstein RE (2000) Chiral self-propulsion of growing bacterial macrofibers on a solid surface. *Phys Rev Lett* 84(7):1627–1630.
10. Vollmer W, Blanot D, de Pedro MA (2008) Peptidoglycan structure and architecture. *FEMS Microbiol Rev* 32(2):149–167.
11. Beeby M, Gumbart JC, Roux B, Jensen GJ (2013) Architecture and assembly of the Gram-positive cell wall. *Mol Microbiol* 88(4):664–672.

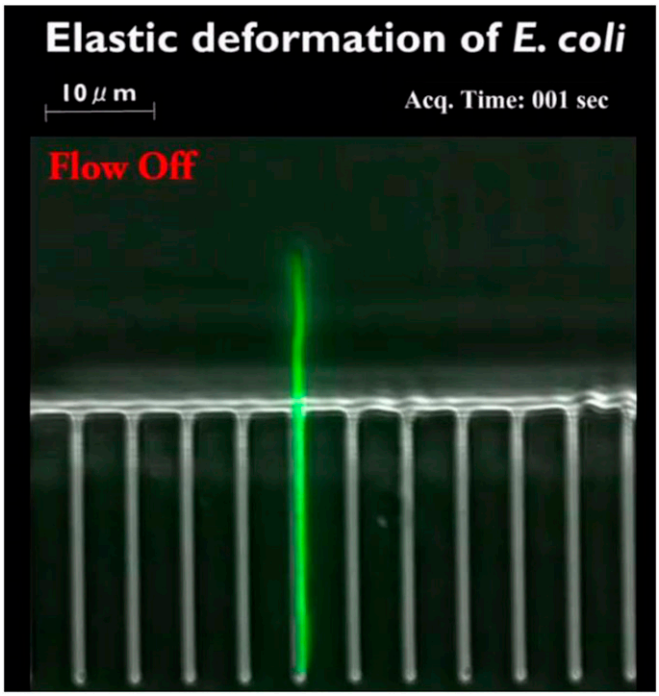

Movie S1. Elastic deformations of an *E. coli* cell. Initially there is no flow in the channel, and the bacterium keeps a straight conformation. Pulses of flow are applied to the cell every several minutes, leading to significant yet fully reversible (elastic) bending of the cell. Details of the experimental system are provided in *Materials and Methods* and *Supporting Information*.

Movie S1

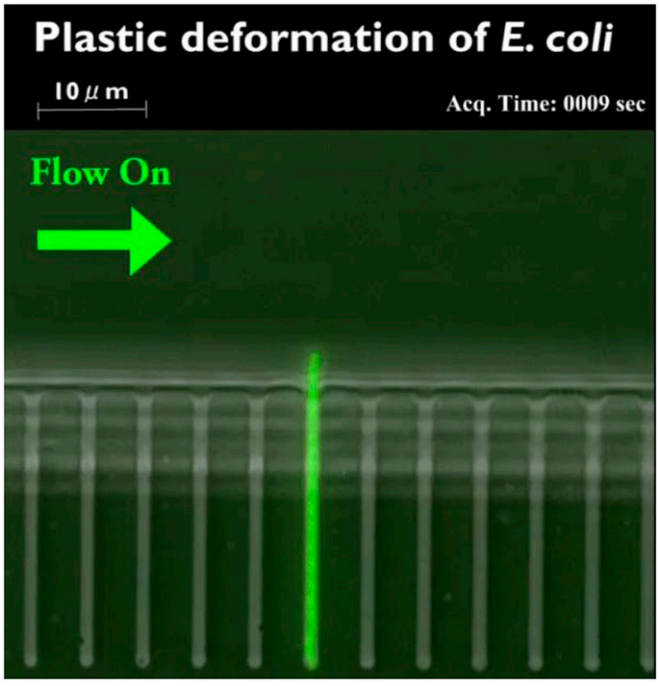

Movie S2. Plastic deformations of an *E. coli* cell. The cell is left to grow in the presence of a constant flow for a period comparable to the cell-doubling time. At time $t = 17$ min the flow is switched off abruptly, yet the cell only partly recovers its bent conformation and remains deformed. Upon further growth, the cell straightens. Details of the experimental system are provided in *Materials and Methods* and *Supporting Information*.

Movie S2